Accepted Manuscript

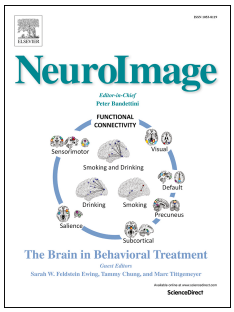

Signal compartments in ultra-high field multi-echo gradient echo MRI reflect underlying tissue microstructure in the brain

Shrinath Kadamangudi, David Reutens, Surabhi Sood, Viktor Vegh

PII: S1053-8119(18)30485-3

DOI: 10.1016/j.neuroimage.2018.05.061

Reference: YNIMG 14986

To appear in: *NeuroImage*

Received Date: 19 January 2018

Revised Date: 24 May 2018

Accepted Date: 25 May 2018

Please cite this article as: Kadamangudi, S., Reutens, D., Sood, S., Vegh, V., Signal compartments in ultra-high field multi-echo gradient echo MRI reflect underlying tissue microstructure in the brain, *NeuroImage* (2018), doi: 10.1016/j.neuroimage.2018.05.061.

This is a PDF file of an unedited manuscript that has been accepted for publication. As a service to our customers we are providing this early version of the manuscript. The manuscript will undergo copyediting, typesetting, and review of the resulting proof before it is published in its final form. Please note that during the production process errors may be discovered which could affect the content, and all legal disclaimers that apply to the journal pertain.

ACCEPTED MANUSCRIPT

Signal compartments in ultra-high field multi-echo gradient echo MRI reflect underlying tissue microstructure in the brain

Shrinath Kadamangudi,[1,2] David Reutens,[1] Surabhi Sood[1] and Viktor Vegh[1]

[1]Centre for Advanced Imaging, University of Queensland, Brisbane, Queensland, AU

[2]Queensland Brain Institute, University of Queensland, Brisbane, Queensland, AU

Total number of words:

Correspondence Address:

Viktor Vegh, Ph.D.

Centre for Advanced Imaging

University of Queensland

Building 57, St Lucia, QLD 4067

Phone:

Fax:

E-mail:

ACCEPTED MANUSCRIPT

ACCEPTED MANUSCRIPT

Abstract

Gradient recalled echo magnetic resonance imaging (GRE-MRI) at ultra-high field holds great promise for new contrast mechanisms and delineation of putative tissue compartments that contribute to the multi-echo GRE-MRI signal may aid structural characterization. Several studies have adopted the three water-pool compartment model to study white matter brain regions, associating individual compartments with myelin, axonal and extracellular water. However, the number and identifiability of GRE-MRI signal compartments has not been fully explored. We undertook this task for human brain imaging data. Multiple echo time GRE-MRI data were acquired in five healthy participants, specific anatomical structures were segmented in each dataset (substantia nigra, caudate, insula, putamen, thalamus, fornix, internal capsule, corpus callosum and cerebrospinal fluid), and the signal fitted with models comprising one to six signal compartments using a complex-valued plane wave formulation. Information criteria and cluster analysis methods were used to ascertain the number of distinct compartments within the signal from each structure and to determine their respective frequency shifts. We identified five principal signal compartments with different relative contributions to each structure's signal. Voxel-based maps of the volume fraction of each of these compartments were generated and demonstrated spatial correlation with brain anatomy.

Keywords: Ultra-high field, GRE-MRI, signal compartments, frequency shift, magnetic susceptibility, tissue microstructure.

ACCEPTED MANUSCRIPT

Introduction

In the brain, regional differences in the echo time dependence of the multi-echo GRE-MRI (mGRE-MRI) signal may reflect the influence of variations in tissue microstructure (Cronin et al., 2017; Schweser et al., 2011a; Sood et al., 2017; Yablonskiy and Haacke, 1994). These effects have been characterized by modelling the mGRE-MRI signals in terms of signal compartments (Du et al., 2007; Hwang et al., 2010; Sati et al., 2013). The compartments are postulated to reflect the micro-scale (< 100μm) magnetic resonance imaging (MRI) voxel constituents, thereby contributing to efforts to map, characterize and quantify brain tissue microstructure (Nam et al., 2015; Thapaliya et al., 2017; Wu et al., 2017).

In myelin water fraction imaging, white matter GRE-MRI signal is modelled by a three-pool model reflecting myelin, axonal and extracellular water pools (Du et al., 2007; Hwang et al., 2010; Nam et al., 2015; Sati et al., 2013; Thapaliya et al., 2017; Wu et al., 2017). Sood et al. (Sood et al., 2017) demonstrated temporal trends in QSM in non-white matter brain regions (i.e. caudate, putamen, substantia nigra, thalamus, pallidum, and red nucleus), and attributed them to variations in cytoarchitecture such as differences in cell density and orientation and iron content (Abduljalil et al., 2003; Drayer et al., 1986; Fukunaga et al., 2010; Schenck and Zimmerman, 2004; Todorich et al., 2009). The signal compartments in non-white matter brain regions remain to be fully explored. We therefore investigated the number of signal compartments in a range of human brain regions (including gray matter, white matter and CSF) using a data driven approach and determined whether signal compartments are shared by different brain regions.

Methods

Data acquisition

The experiment protocol was approved by the University of Queensland Human Research Ethics Committee. Informed consent was provided by seven healthy adult volunteers of mean age of 33 ± 3 years. *In vivo* brain imaging was conducted on a 7T whole-body MRI scanner (Siemens Healthcare, Erlangen, Germany) equipped with a 32-channel head coil (Nova Medical, Wilmington, Massachusetts). A 30 echo 3D gradient recalled echo scan with monopolar echo readout was acquired with the following acquisition settings: TE_1 = 2.04 ms and echo spacing of 1.53 ms, TR = 51 ms, flip angle = 15^o, voxel size = 1 × 1 × 1mm, matrix size = 210 × 168 × 144, bandwidth = 850Hz/voxel and phase encoding direction acceleration = 2. Data was acquired in 6 min 13 s.

Signal processing and quantitative susceptibility mapping

The magnitude image of each channel was used to form a channel mask using the BET tool provided as part of MIPAV 7.3.0 (http://mipav.cit.nih.gov/). The result was read into MATLAB 2015b (The MathWorks, Natick, Massachusetts) from which a binary mask was created. STI Suite V2.2 (http://people.duke.edu/_cl160/) was used to process susceptibility maps in a channel-by-channel manner, as described previously (Bollmann et al., 2015). iHARPERELLA (background phase removal) and iLSQR in STI Suite were used to generate 3D susceptibility maps for each echo time.

Region-of-interest selection

Nine brain regions were considered in this study: the caudate, putamen, fornix, corpus callosum, internal capsule, insula, substantia nigra, thalamus, and cerebrospinal fluid (CSF). The white matter regions (corpus callosum, internal capsule, and fornix) were selected to enable comparison with the results of previous myelin water fraction imaging studies. Five

sub-cortical gray matter regions, namely the caudate, putamen, insula, substantia nigra, and thalamus were selected as a representative sample of overall sub-cortical gray matter structures. Manual segmentation was performed in MIPAV (illustrated in Fig. 1). To minimize the influence of partial volume effects, segmentation boundaries were kept at least two voxels away from the boundary with adjacent regions.

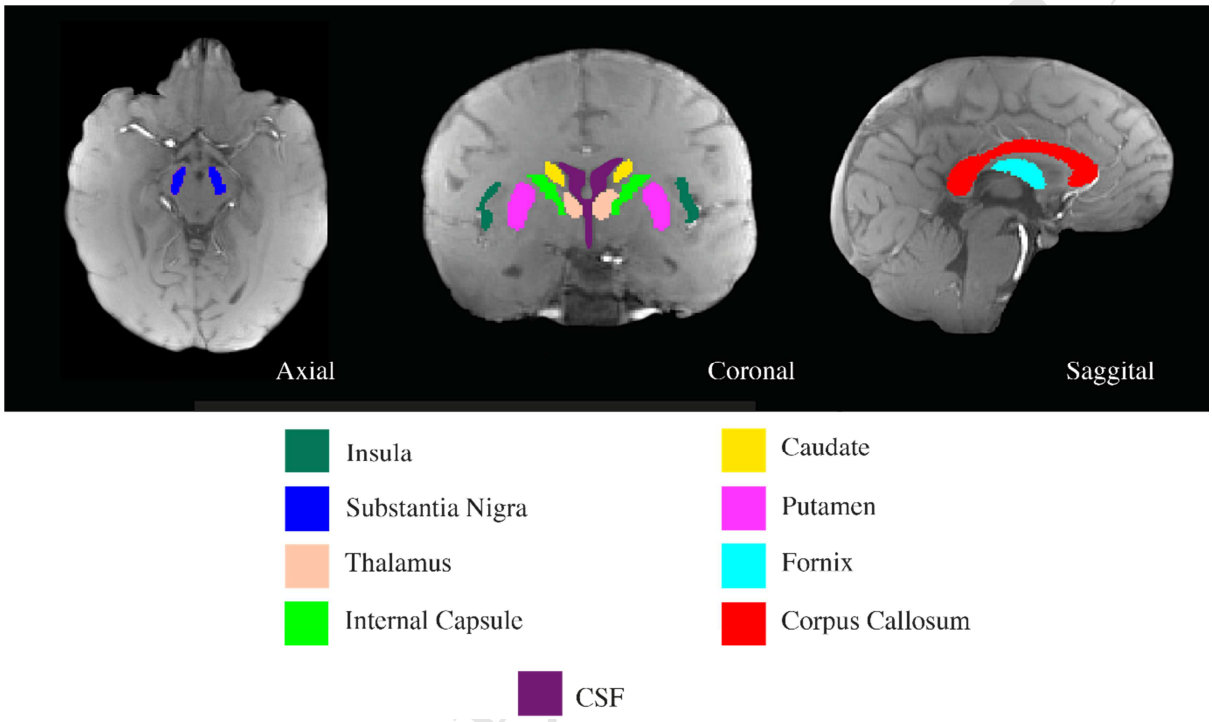

Fig. 1. Illustration of the brain regions investigated.

Complex signal generation

To reduce the influence of non-local magnetic fields, we converted tissue phase to quantitative susceptibility maps which were used to estimate frequency shift to overcome drawbacks of working with tissue phase directly (Wu et al., 2017) using:

$$\Delta f = \chi \frac{\gamma B_0}{2\pi},$$

where χ denotes the magnetic susceptibility value generated using the STI Suite pipeline, γ is the gyromagnetic ratio of hydrogen and B_0 = 7T (Reichenbach et al., 1997;

Schweser et al., 2011; 2016). The complex signal at each echo time [$S_m(t)$] was generated using magnitude (A_m) and frequency shift (Δf_m), averaged across voxels within each region:

$$S_m(t) = A_m(t)e^{-i2\pi\Delta f_m t}.$$

Temporal profiles of the multi-echo magnitude and susceptibility signal for all ROI have been demonstrated previously (Sood et al., 2017). Note, we used the *–i* reference frame here whereas previously the *i* reference frame was used, resulting in a difference in sign of compartment frequency shifts.

Signal compartmentalization

In accordance with previous studies (Li et al., 2015; Nam et al., 2015; Sati et al., 2013; Wu et al., 2017), compartments of the complex GRE-MRI signal were modelled using a relaxation modulated amplitude modulated plane wave formulation.

$$S(t) = \sum_{i=1}^{N} A_i(t)e^{-\frac{t}{T^*_{2,i}} - i2\pi\Delta f_i t},$$

where S(t) is the signal, N is the total number of signal compartments used to fit the measured signal, $T^*_{2,i}$ is the compartment spin-spin relaxation time, in seconds, in the presence of field inhomogeneities and Δf_i is the compartment frequency shift. We considered the cases of N = 1 to 6. Any particular brain region was found to have a maximum of three compartments (refer to Table 2) and, have provided values for an additional three compartments to visualize the convexity of information loss due to overfitting. Phase shift was not required as background field had been removed (Li et al., 2014). As magnetic field changes introduced by micro-scale (< 100µm) effects were assumed to be confined to millimeter-scale (100µm – 1000µm) voxels, a dipole representation for signal compartments was not used (Chen et al., 2013; Sood et al., 2017).

Non-linear least squares fitting implemented in MATLAB (Mathworks, Natick, MA, USA) was used to estimate model parameters (A_i, $T^*_{2,i}$, and Δf_i). Initial values and

optimization search ranges are summarized in Table 1. Fitted parameters were stable despite varying initial values (see Supplementary Table 1).

Table 1
Initial values and search range used to estimate parameters of one to six compartment signal models. $S(TE_1)$ denotes the magnitude of the first-echo signal. $N = 1\ to\ 6$ (number of compartments). The maximum number iterations was *N* x 40,000.

	A (a.u.)	T_2^* (ms)	Δf (Hz)
Initial value	$\frac{\lvert S(TE_1)\rvert}{N}$	30	0
Lower bound	0	0	-150
Upper bound	$2 \times \lvert S(TE_1)\rvert$	200	150

ACCEPTED MANUSCRIPT

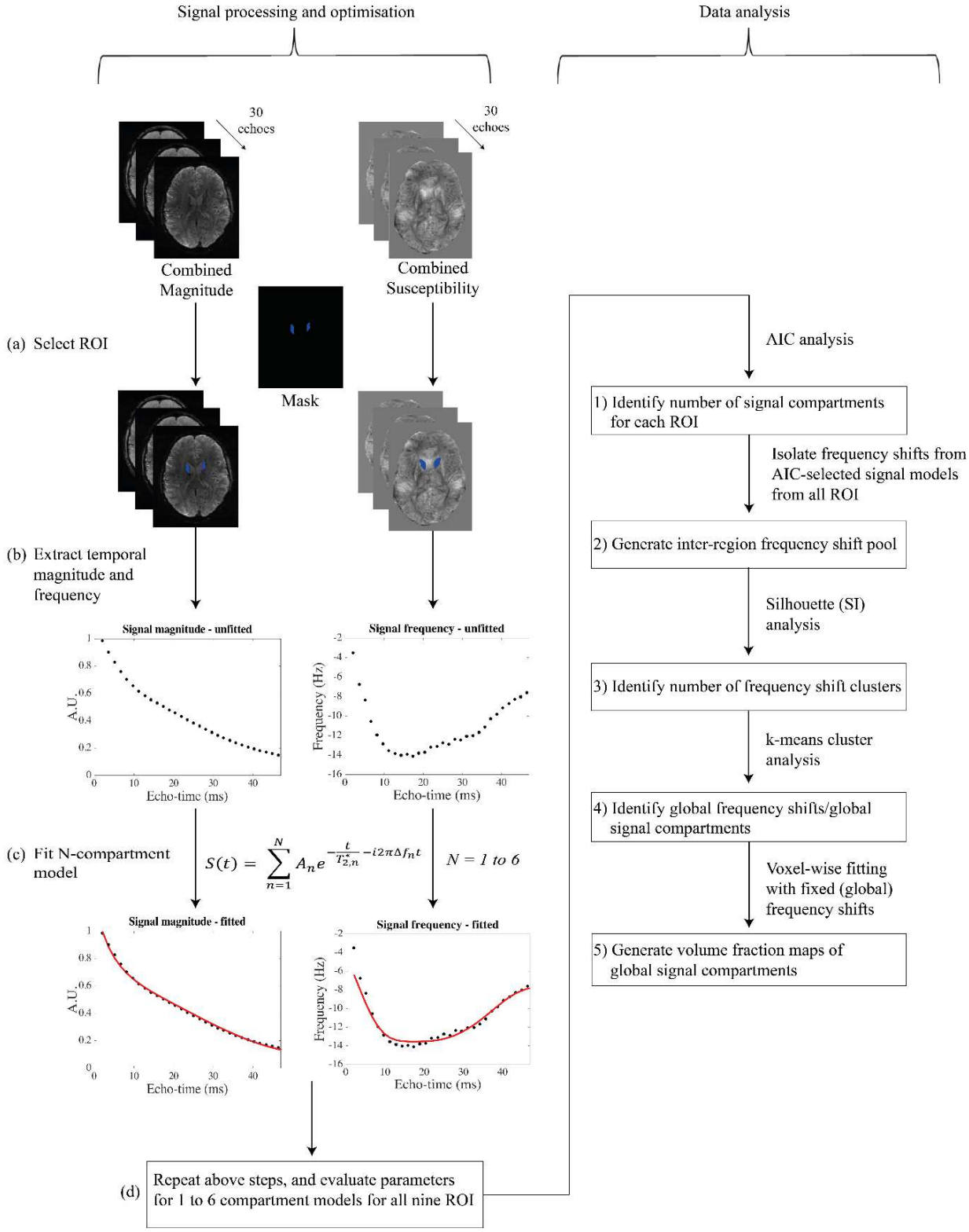

Fig. 2. Data processing and analysis pipeline—example given for the caudate in one participant. (a) ROIs were selected from combined magnitude and combined susceptibility data (mask manually generated via magnitude images). (b) Averaged magnitude and susceptibility values were calculated for each ROI; averaged susceptibility values were converted to frequency shifts at each echo time. (c) The complex signal was generated using as a function of magnitude, frequency shift, and echo-time, and fitted to a multi-compartment (one to six compartment) model. (d) The most parsimonious compartment models were selected via the AIC for further analysis.

Model selection and cluster analysis

Out of the seven datasets, we used only the first five participants' data for model selection and cluster analysis. The other two participant datasets were used for validation. Achieving model parsimony, or the ideal balance between bias and variance, requires a model to exhibit accuracy and simplicity in describing the measured data (Vandekerckhove et al., 2014). The Akaike Information Criteria (AIC) was used to control overfitting in model selection (Akaike, 2011; Naik et al., 2007). The AIC fine tunes model parsimony by reinforcing improvements in quality-of-fit and penalising an increasing number of parameters. Further, the AIC allows the comparison of two or more models in describing the measured data via a maximum likelihood estimation. When fitting a model using least squares regression, the likelihood function can be estimated by the residual sum of squares (RSS) of the least squares fit, yielding:

$$AIC = n \log\left(\frac{RSS}{n}\right) + 2k,$$

where *n* is the number of independent measurements, and *k* represents the number of unknown parameters. When implementing the AIC for a small sample, or measurement (i.e. n/k < 40) size, an additional bias correction penalty term is required (Bedrick and Tsai, 1994; Burnham and Anderson, 2004); this yields a 'corrected' AIC (AIC_c) metric:

$$AIC_c = AIC + \frac{2k(k+1)}{n-k-1}.$$

The model with an AIC value lower than the two adjacent models is the most parsimonious choice. Note, the first lowest AIC value should be chosen to avoid overfitting. To determine whether signal compartments were shared between different brain regions, we

performed a k-means cluster analysis of compartment frequency shifts associated with the most parsimonious model for each region (Arthur and Vassilvitskii, 2007). These compartment frequency shift clusters represent commonly occurring components of the mGRE-MRI signal phase across the nine regions considered; as such, these clusters are herein referred to as 'global frequency shifts', each of which correspond to a 'global signal compartment'. It is important to note that global frequency shifts and signal compartments have been derived from a subset of brain regions and additional ones may exist in brain regions not considered in this study. The number of clusters was determined using a silhouette (SI) analysis using the k-means and SI function tools in MATLAB. Implementation of model selection and cluster analysis steps are summarized in Fig. 2.

Connection map

Based on the first five participants' data, an analytical connection map was created to visualize how frequency shifts of signal compartments of each ROI linked to frequency shifts associated with the global signal compartments. This allowed us to understand the extent to which global signal compartments contributed to individual ROIs. This analysis was performed by (1) arranging the global compartment frequency shifts on a frequency spectrum (set to a loose range so as to include all values), (2) plotting volume fraction weighted shape representations of within-region compartment frequency shifts on the frequency spectrum, (3) linking the within-region compartment frequency shifts to their respective brain regions, and (4) ordering the brain regions by minimizing the path length of their connections. All components of this analysis were carried out using standard illustration tools in Adobe Illustrator® CC 2015 (Adobe Systems, San Jose, CA, USA).

Generating volume fraction maps based on compartment frequency shifts

The complex valued voxel signal was modelled using a five-compartment model with frequency shifts fixed to the five global frequency shifts identified by the cluster analysis (Fig. 3). The standard error (SER) was calculated for each multi-compartment fit by (1) normalizing the real and imaginary residual sum of squared errors for each echo time, and (2) summing the normalized residual squared errors across all echo times. We performed two levels of validation. Firstly, we generated a volume fraction map for the first participant and assessed whether fixing of frequency shifts results in representative volume fractions. Secondly, we resolved volume fraction maps based on datasets not used in the cluster analysis. We have defined three levels of matchings between volume fractions obtained using region-based and voxel-based analyses. In the results we use the ### symbol to indicate that the largest volume fractions and their ordering correspond between the region-based and voxel-based analyses (i.e. very good match). The symbol ## identifies brain regions for which the largest volume fraction compartments correspond (i.e. good match). Finally, # has been used to highlight the brain region for which one compartment volume fraction is mismatched (i.e. partial match).

Results

Information criteria indicate a unique number signal compartments for individual brain regions

Table 2
AIC values for one to six compartment models. Results from the one (1C) to six (6C) compartment model AIC analysis for each ROI. The smallest AIC value, used for model selection, is in bold face.

	Number of compartments					
	1C	**2C**	**3C**	**4C**	**5C**	**6C**
Caudate	110	103	**95**	103	121	149
Putamen	121	104	**103**	109	126	157
Fornix	98	**86**	93	89	108	141
CC	99	90	**79**	85	103	134
IC	114	103	**77**	88	96	127
Insula	127	**110**	113	118	136	168

SN	81	80	**75**	81	99	127
Thalamus	69	**67**	71	72	90	121
CSF	105	**98**	102	113	132	166

The AIC analysis suggests the presence of more than one signal compartment for all regions investigated (Table 2). Two signal compartments were identified for the fornix, CSF, insula and thalamus regions. Three signal compartments were selected for the caudate, putamen, corpus callosum, internal capsule and substantia nigra. Table 3 provides individual parameter values obtained using the AIC-selected compartment models.

Cluster analyses reveal global inter-region signal compartments

Via the SI analysis, five frequency shift clusters were identified across brain regions considered (Table 4). Fig. 3 elucidates the clustering of compartment frequency shifts, ascertained via k-means clustering. The five frequency shift clusters exhibited cluster centroids at -27.5Hz, -8.4Hz, 4.6Hz, 17.8Hz, and 29.5Hz; each centroid was labelled as a 'global frequency shift'. Fig. 3 displays the distribution of signal compartments across brain regions according to frequency shift.

Table 3
Estimated parameters for AIC-selected signal compartment models for each brain region. Frequency shifts have been highlighted using bold face, and volume fraction of each compartment is expressed as a percentage. Compartments are ordered from largest to smallest volume fraction occupied. A1-A3 are compartment volume fractions, Δf_1-Δf_3 are compartment frequency shifts, and SER is the standard error of fit.

	A_1	Δf_1 (Hz)	A_2	Δf_2 (Hz)	A_3	Δf_3 (Hz)	SER (%)
Caudate	56%	**9.7**	25%	**22.1**	19%	**-26.8**	7.4
Putamen	48%	**3.9**	27%	**15.6**	25%	**29.5**	9.6
Fornix	86%	**-5.9**	14%	**6.6**			6.8
CC	37%	**1.0**	32%	**8.1**	31%	**-31.5**	3.9
IC	71%	**-11.0**	22%	**-24.1**	7%	**17.8**	3.7
Insula	52%	**-8.4**	48%	**4.7**			13.2
SN	36%	**3.4**	33%	**17.5**	32%	**7.2**	4.6
Thalamus	51%	**3.5**	49%	**-1.0**			3.6
CSF	87%	**3.6**	13%	**16.1**			10.3

Table 4
Mean silhouette (SI) values for AIC-selected compartment models. The bold highlights the largest SI value used to define the number clusters.

No. of clusters	**Mean SI**
1	N/A

2	0.77
3	0.76
4	0.83
5	**0.86**
6	0.81
7	0.84
8	0.82
9	0.84
10	0.83

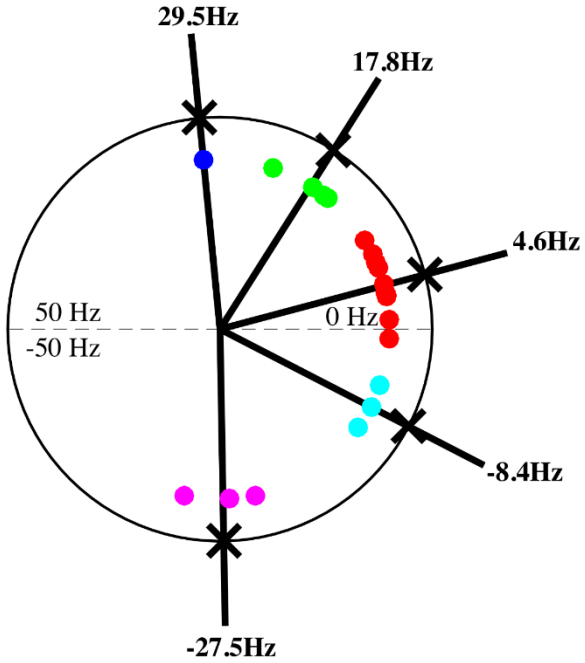

Fig. 3. Clustering results obtained using the AIC-selected signal compartment frequency shifts. Distinct frequency shift clusters are identified using different colors, and cluster centroid values are displayed as radial lines intersecting the circle at points marked by the cross.

ACCEPTED MANUSCRIPT

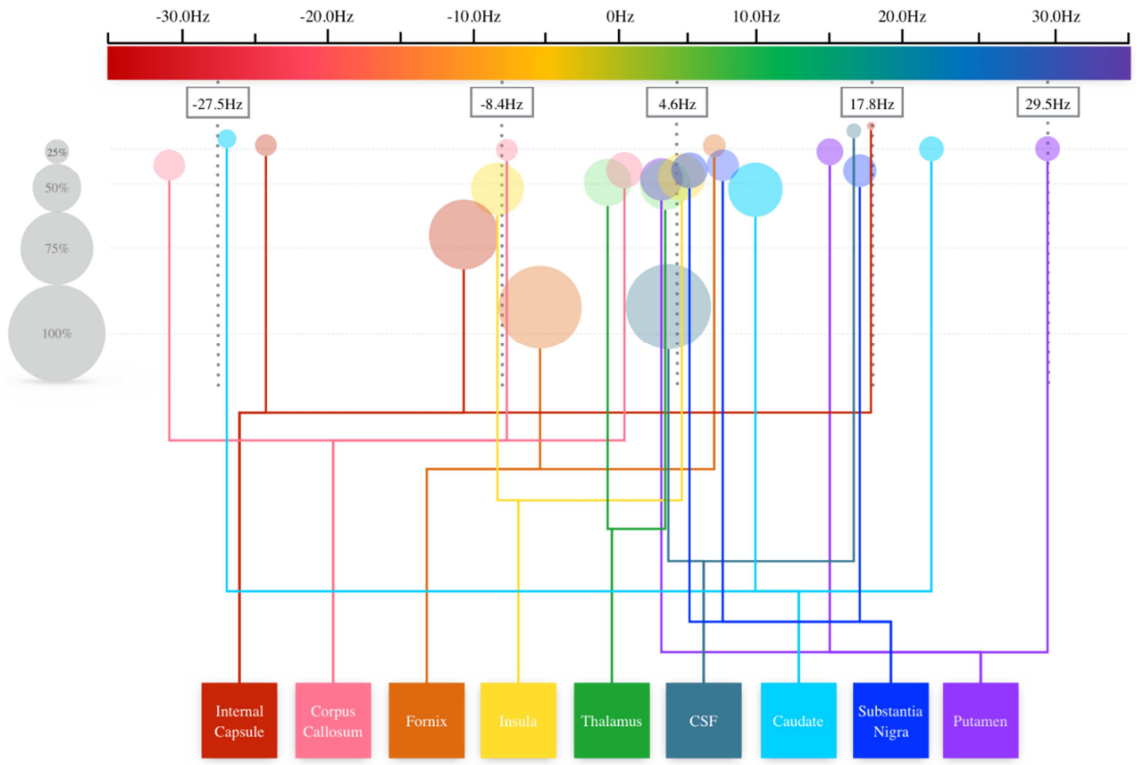

Fig. 4. A connection map of compartment frequency shifts and volume fractions for all ROI. The AIC-based centroids identified using cluster analysis are shown on the frequency axis, and the size of the compartments represented using different sized circles are presented vertically. Each region has been connected to their respective compartment frequency shift values. The regions have been arranged in an order which minimizes the number of overlapping lines, simply to assist with the visualization of signal compartment volume fractions and their frequency shifts.

Volume fraction maps of global signal compartments

ACCEPTED MANUSCRIPT

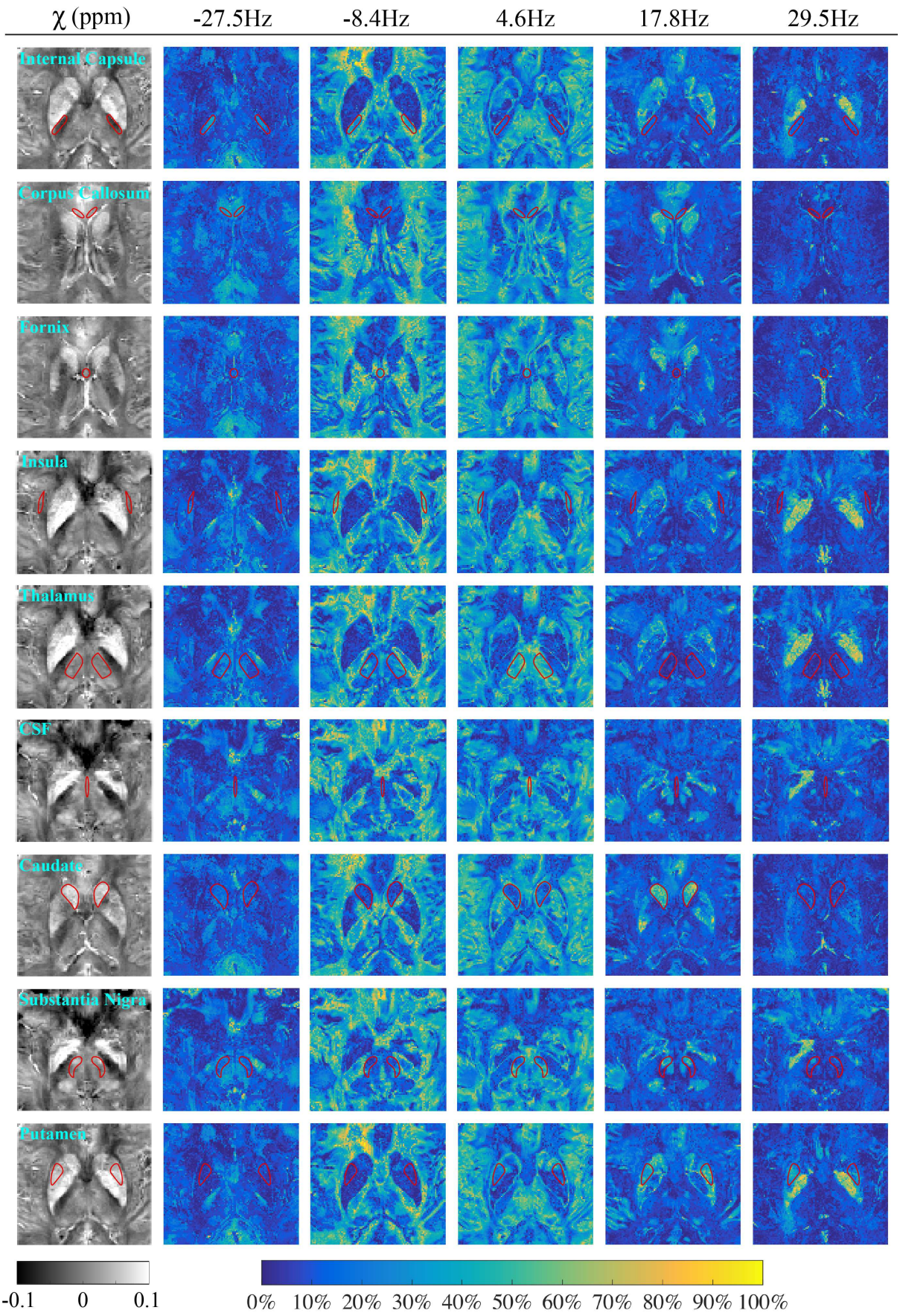

Fig. 5. Voxel-wise parametric mapping of global signal compartment volume fractions for the first participant (P1). Corresponding 11th echo time magnetic susceptibility images (in ppm) are provided in the first column for comparison. Representative axial slices for each ROI, marked by the area

inside the red outlines, were chosen for mapping based on best structural visibility. The gradient color bar indicates the volume fraction of each frequency shift contribution.

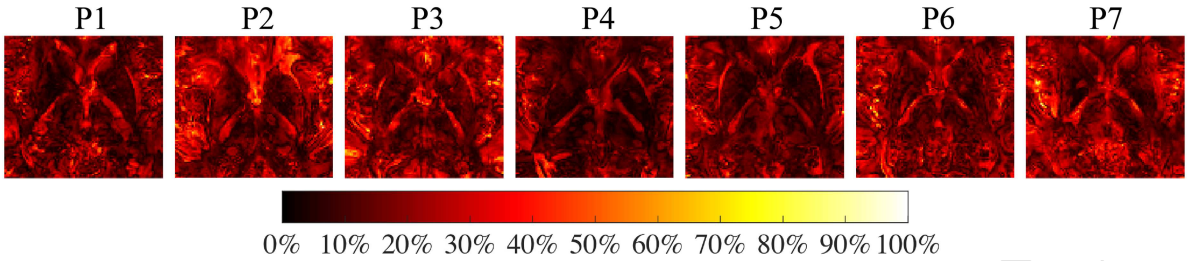

Fig. 6. Fitting error maps for five participants (P1 – P5) used and two participants (P6 – P7) not used in the cluster analysis. SER values for each voxel fit were normalized with respect to the largest SER value within representative slices of similar anatomical location, and are presented as a percentage for interpretive benefits.

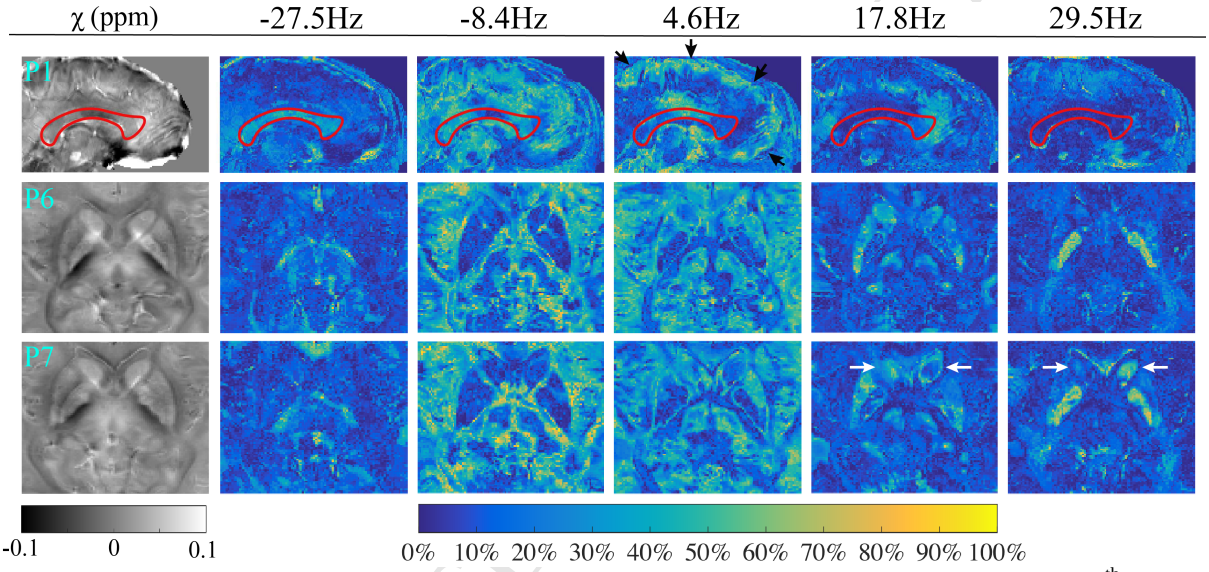

Fig. 7. Additional volume fraction maps for participants P1, P6 and P7 with corresponding 11th echo time magnetic susceptibility maps (in ppm) in the first column. (P1) Zoomed in view in the sagittal orientation to visualize compartment volume fraction map changes. The corpus callosum has been highlighted in red, and the black arrows depict the subarachnoid space, a key area for cortical CSF absorption. Results for (P6) and (P7) are volume fraction maps for participants not included in the cluster analysis. The arrows point to the region of the caudate where volume fraction changes are present across the 17.8 Hz and 29.5 Hz frequency shift compartments.

Fig. 5 shows volume fraction maps of individual signal compartments. We observe a close correspondence of the analytically calculated within-region compartment model parameters (refer to Table 3) to the spatial distribution of signal compartments across gray and white matter regions (Fig. 5). For example, in the putamen, we observe three signal compartments with frequency shifts at 3.6Hz, 15.9Hz, and 29.5Hz; these signal compartments fall within the respective global signal frequency shift clusters of 4.6Hz, 17.8Hz, and 29.5Hz. When inspecting the volume fraction maps for this region, we observe a

ACCEPTED MANUSCRIPT

high degree of localization corresponding to the three global signal compartments (Fig. 5). A similar correspondence of model-based parameters to volume fraction maps can be observed in white matter regions, such as the internal capsule. The signal compartment with the highest volume fraction in this region falls within the -8.4Hz global frequency shift cluster (Fig. 3); this result corresponds to a high representation of the -8.4Hz global signal compartment, as displayed in Fig. 5. The other two signal compartments in this region, with frequency shifts of -24.1Hz (22%) and 17.8Hz (7%) corresponding to the -27.5Hz and 17.8Hz global frequency shifts, also display regional localization, but to a lesser degree than the highest volume fraction compartment (compare Table 3 and Fig. 5). Such a correspondence can also be observed within the CSF (refer to P1 in Fig. 7). The largest within-region compartment frequency shift, resolved at 3.6Hz (87%) (Table 3), falls within the 4.6Hz global frequency shift cluster; this global frequency shift exhibits a notably high volume fraction within the CSF (Fig. 5). Overall, the volume occupancy of the global signal compartments localize in a structured manner across the brain regions investigated.

Normalized SER distributions for voxel-wise volume fraction estimation are displayed in Fig. 6 for all seven participants (P1—P5). Of note, the fitting error distributed similarly across all participants and a low fitting error was present within the corpus striatum (caudate, putamen, and globus pallidus), whilst higher errors were present in the surrounding white matter structures (corpus callosum, internal capsule, and fornix).Lastly, the fitting errors within the cortical areas do not seem to obviate localization to any particular structure, but nonetheless remain higher than sub-cortical regions.

The corpus callosum and CSF regions are difficult to visualize in the axial orientation shown in Fig. 5. Thus, we provide findings in the sagittal view for the first participant (Fig. 7 and P1). In addition, we have included results from two additional participants not used in the cluster analysis (see Fig. 7 and P6 and P7). Whilst data from these two additional participants

were not used to define the fixed frequency shifts, the volume fraction maps correspond closely to those shown in Fig. 5. For P7 we point out the region of the caudate where a discrepancy is present in the volume fraction maps across the 17.8 Hz and 29.5 Hz signal compartments. This finding is in agreement with those presented in Fig. 4, wherein the caudate frequency shift presents between the 17.8 Hz and 29.5 Hz frequency shifts. Therefore, we could expect elevated volume fractions in the 17.8 Hz and 29.5 Hz frequency shift compartments.

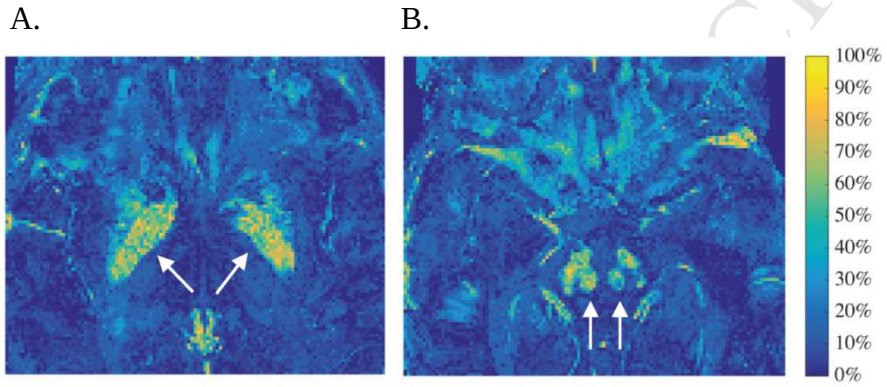

Fig. 8. Localization of high frequency (29.5Hz) signal compartment in the globus pallidus (A) and red nucleus (B), as indicated by the tailed arrows.

By fixing global frequency shifts in the compartment model, we were able to identify two sub-cortical areas which exhibited an apparent image contrast and remarkably high volume fraction of the 29.5Hz frequency shift compartment (see Fig. 8). These areas delineate clearly (A) the globus pallidus and (B) the red nucleus, as indicated by the arrows. Interestingly, neither of these structures were used to identify the five global frequency shifts.

Table 5 summarizes the volume fraction and T_2^* values for each of the brain regions investigated based on data generated using fixed frequency shifts in the voxel-wise fitting. Note, we have bolded numbers corresponding to compartments where we expect the contributions based on the cluster analysis results. A correspondence between volume fractions presented in Tables 3 and 5 is present in all nine brain regions. Six out of the nine brain regions had either a very good or good match, whilst three regions matched partially.

The compartment T_2^* values provided in Table 5 illustrate the variability within and across regions, and the 4.6 Hz frequency shift compartment in general has the largest T_2^* value. Overall, our results suggest that voxel-wise mappings reflect volume fractions found using the region-based analysis.

Discussion

We explain temporal variations in mGRE-MRI data acquired at 7T using complex-valued signal compartments. Five global signal compartments were shared across a variety of gray (caudate, putamen, insula, thalamus, substantia nigra) and white (corpus callosum, internal capsule, and fornix) matter regions and CSF.

Table 5
Region-based mean and standard deviation frequency shift compartment volume fractions and T_2^* values. The mean of voxel values in each region was calculated and then averaged across participants. The standard deviation reflect the variation across participants. We have defined three levels of matching between voxel-wise volume fractions and region-wise volume fractions (Table 3): ### very good, ## good and # partial match with compartments identified in Table 3. Values in bold indicate locations where we expect contributions based on the region-based cluster analysis. The italicized values for the CSF and caudate indicate a potential misalignment due to the use of discrete frequency shifts.

Compartment	*-27.5Hz*	*-8.4Hz*	*4.6Hz*	*17.8Hz*	*29.5Hz*
			Volume fraction (%)		
IC[#]	**14.8** ± 9.5	**31.0** ± 12.6	17.0 ± 5.2	**16.4** ± 4.8	20.9 ± 10.3
CC[###]	**26.0** ± 5.1	**25.1** ± 9.1	**30.9** ± 4.1	13.0 ± 5.2	5.2 ± 1.3
Fornix[###]	16.2 ± 3.2	**36.2** ± 16.4	**29.6** ± 12.4	11.1 ± 6.4	7.0 ± 3.1
Insula[###]	8.6 ± 3.0	**43.3** ± 6.9	**24.8** ± 6.6	12.1 ± 0.4	11.2 ± 2.6
Thalamus[###]	11.9 ± 4.3	**29.3** ± 8.5	**40.3** ± 3.2	9.2 ± 21.0	9.2 ± 3.2
CSF[##]	18.4 ± 5.2	*24.9* ± 10.6	**28.3** ± 4.0	**18.7** ± 9.4	9.7 ± 3.6
Caudate[##]	**12.0** ± 2.2	18.3 ± 9.8	**27.0** ± 5.3	**28.9** ± 12.1	*13.8* ± 5.8
SN[#]	17.1 ± 7.7	26.5 ± 10.4	**23.0** ± 7.3	**18.1** ± 4.2	15.3 ± 9.3
Putamen[#]	7.1 ± 2.2	26.2 ± 13.5	**29.9** ± 10.2	**18.6** ± 7.8	**18.2** ± 7.0
			T_2^* (ms)		
IC	**9.0** ± 6.3	**37.0** ± 15.9	32.2 ± 22.6	**24.7** ± 14.5	7.4 ± 3.7
CC	**14.8** ± 3.1	**38.2** ± 11.8	**76.0** ± 9.9	45.5 ± 41.0	3.9 ± 1.7
Fornix	23.2 ± 7.9	**62.9** ± 43.2	**74.5** ± 48.1	12.3 ± 14.6	8.7 ± 9.5
Insula	2.8 ± 3.2	**60.6** ± 6.1	**78.7** ± 14.7	18.5 ± 6.2	8.1 ± 2.3
Thalamus	15.0 ± 4.8	**57.4** ± 12.9	**74.0** ± 10.5	25.7 ± 4.9	7.3 ± 3.9
CSF	23.7 ± 12.9	51.0 ± 20.3	**119.2** ± 45.4	**60.2** ± 38.5	17.7 ± 14.7
Caudate	**10.2** ± 2.9	28.1 ± 21.5	**56.7** ± 28.9	**39.0** ± 5.9	18.0 ± 6.4
SN	13.2 ± 7.8	28.0 ± 8.7	**49.0** ± 14.6	**35.3** ± 14.8	11.9 ± 8.7
Putamen	3.8 ± 2.5	42.3 ± 31.1	**68.0** ± 29.2	**47.7** ± 18.9	**13.1** ± 2.3

Evaluating signal compartments in a data driven framework

Previous studies which use the three-compartment water fraction model to explain temporal trends in mGRE-MRI data have been confined to white matter regions (Li et al., 2015; Nam et al., 2015; Sati et al., 2013; Wu et al., 2017). Frequency shifts in 'extracellular' fluid and CSF are commonly assumed to be zero (Alonso-Ortiz et al., 2017; Nam et al., 2015; van Gelderen et al., 2012; Wu et al., 2017). A recent study performed by Straub et al. (2017) found the CSF to be a stable and robust region for susceptibility referencing in healthy participants; the authors report a volume susceptibility of 0.010ppm within this region, corresponding to a frequency shift of 3.0Hz at 7T after converting in accordance with Eq. 1. In line with these findings, the frequency shift we observe in CSF, suggest that assuming null field effects of extracellular tissue may introduce bias (Table 3 and Fig. 5).

Unlike previous studies (Lee et al., 2017; Li et al., 2015; Sati et al., 2013; Sood et al., 2017), we used the AIC for model selection, thereby controlling for overfitting (Hurvich and Tsai, 1989; Snipes and Taylor, 2014; Vandekerckhove et al., 2014). Data driven methods were used to extract global signal influences across brain regions (refer to Table 2, Table 4, and Fig. 3). Five of the nine regions investigated contained three signal compartments but the frequency shifts of the compartments differed between regions (Table 2). In some regions such as CSF, thalamus, and insula, as few as two compartments were sufficient to model the signal (Table 2).

Trends in compartment frequency shifts reflect underlying tissue microstructure

The allocation of brain regions on the signal compartment relationship map suggests an underlying link between mesoscopic tissue properties and signal compartment frequency shifts. We observed an underlying microstructural pattern by arranging brain regions in Fig. 4 such that path lengths of connections were minimized. As the nervous system's primary relay

centre for ascending and descending pathways (Sherman, 2016), the thalamus comprises a diverse regional cytoarchitecture; a combination of paramagnetic and diamagnetic inclusions, as well as, multiple fiber orientations could result in attenuated susceptibility effects and a low number of signal compartments resolved subsequently (see Fig. 4 and Table 3). Typically identified as gray matter structures, the insula, caudate, putamen, and substantia nigra are commonly characterized by densely packed neuronal cell bodies, synaptic terminals, and weakly myelinated regions of the axon hillock (Purves et al., 1997). As a whole, these gray matter structures exhibit multiple within-region compartment frequency shifts around 17.8Hz and 4.6Hz, and appear adjacent on the relationship map (Fig. 4). The three white matter regions investigated (internal capsule, corpus callosum, and fornix) also group closely on the relationship map around the -27.5Hz and -8.4Hz frequency shift signal compartment (Fig. 4). These results extend prior findings which report a bulk diamagnetic susceptibility effect, measured as a reduced resonant frequency within white matter regions (Duyn et al., 2007; Fukunaga et al., 2010; Lee et al., 2012).

In addition, Thapaliya et al. (2017) studied compartment model parameters from the genu to the splenium of the corpus callosum in the mid-sagittal plane. Whilst there are methodological differences between the studies, such as frequency shifts generated directly from phase values versus from susceptibilities and referencing to extracellular water versus no specific referencing, three specific observations can be made. Firstly, our findings confirm the presence of three compartments in the corpus callosum. Secondly, our frequency shift separations between compartments reported in Table 3 are similar to those reported by them (32.5 Hz is in the 10-38 Hz range, and 7.1 Hz is in the 6-12 Hz range). Thirdly, they reported a larger axonal water fraction than myelin water fraction, and significantly smaller T_2^* value for the myelin compartment, both of which agree with our findings in Table 5.

ACCEPTED MANUSCRIPT

The global frequency shifts ascertained from our data driven analysis allowed us to resolve volume fractions of identified mGRE-MRI signal influences (Fig. 4). Representative image slices for one participant were mapped to allow a ROI-based analysis of spatial distributions of global signal compartments (Fig. 4). The error distributions, provided in Fig. 6, demonstrate a similar quality of voxel-wise fitting across all participants. This result validates the generalizability of the extent to which these global signal compartments influence the mGRE-MRI signal. Furthermore, this exercise validated our analytical evaluation of inter-region signal compartment trends (Fig. 4), and elucidated the utility of providing new quantitative contrast mechanisms for clinical and empirical purposes.

Considering the biophysical origins of signal compartments and respective frequency shifts

The 29.5Hz signal compartment most likely reflects the paramagnetic influence of non-heme tissue iron (Deistung et al., 2013; Drayer et al., 1986; Fukunaga et al., 2010; Haacke et al., 2007, 2007; Schenck and Zimmerman, 2004; Schweser et al., 2011b, 2012). This compartment was dominant in the putamen, substantia nigra, caudate, globus pallidus and red nucleus (refer to Fig. 5 and Fig. 8), regions known to have a high iron concentration (Aquino et al., 2009; Drayer et al., 1986; Hallgren and Sourander, 1958; Schweser et al., 2011).

A high volume fraction of the 17.8Hz signal compartment also occurred in the caudate, putamen, and substantia nigra (see Figs. 5 and 7) and may reflect iron in the ferrous state. Trace amounts of ferritin and transferrin bound iron have been reported in the CSF (Khalil et al., 2014; Straub et al., 2017) and may explain the minor signal compartment (13%) near the 17.8Hz cluster in CSF (Figs. 5 and 7, and Table 5). The largest signal compartment in CSF was the 3.6Hz frequency shift compartment (87%). This is consistent with the finding by Straub et al. (2017) of a bulk CSF frequency shift of 3.0 Hz at 7T.

The 3.6Hz frequency shift of the signal compartment in CSF lies in close proximity to the 4.6Hz global frequency shift cluster (Fig. 4). Though CSF is not found within the interstitial brain parenchyma (Jessen et al., 2015), the parameter values for this compartment are suggestive of extracellular water. The magnetic properties of the extracellular space have been related to cerebrospinal fluid in previous studies (Li et al., 2015). Distributed throughout extracellular space are dynamic quantities of solvated salts, proteins and glucose; these ionic and macromolecular moieties could be captured collectively as a signal compartment, previously unobservable due to decreased sensitivity to susceptibility influences at lower field strengths (Alonso-Ortiz et al., 2017; Duyn et al., 2007; van Gelderen et al., 2012; Wharton and Bowtell, 2012). A lack of structural coherence amidst these inclusions, however, provide reason as to why this signal compartment exhibits the lowest magnitude of induced field change.

Previous studies that used the three-pool model report frequency shifts for axonal water in a range comparable to the -8.4Hz signal compartment identified in our study (Li et al., 2015; Sati et al., 2013). Sati et al. (2013) report axonal water frequency shifts at -6.0Hz in the optical radiatum and -4.1Hz in the splenium of the corpus callosum; frequency shifts in the same range -6.3Hz in the optic radiatum and -6.5Hz in the splenium of the corpus callosum were observed by Li et al. (Li et al., 2015). The orientation of axons with respect to the scanner field influences frequency shift (Sati et al., 2013) Our results align with previous studies which report negative echo-time dependent frequency differences in orientation dependent white matter structures (Duyn et al., 2007; Duyn and Schenck, 2017; Lee et al., 2012; Liu et al., 2011; Wharton and Bowtell, 2012).

Prior studies report diamagnetic susceptibility properties referenced to CSF for proteins in gray and white matter (He and Yablonskiy, 2009; Leutritz et al., 2013; Luo et al., 2010; Zhong et al., 2008). In an early study by Hong et al., (1971), rhodopsin, a G-protein-

coupled receptor (GPCR) was reported be the primary constituent for orientation dependent magnetic susceptibility effects in rod cells, in comparison to phospholipid molecules. Recent studies extend these findings by reporting diamagnetic susceptibility properties for proteins in gray and white matter brain regions (referenced to CSF), ranging on the order of parts per billion (ppb) in the susceptibility domain and Hertz (Hz) in the frequency domain, at 7T (He and Yablonskiy, 2009; Leutritz et al., 2013; Luo et al., 2010; Zhong et al., 2008). The -27.5Hz cluster centroid, identified in Fig. 3 and mapped in Fig. 4, may reflect the bulk susceptibility effect arising from the microscopic arrangement of proteins in the brain. The bulk diamagnetic susceptibility effects of lipids and proteins, however, were reported to field effects of similar magnitude, but in the opposite direction, in comparison to chemical exchange effects (Leutritz et al., 2013). Thus, though the bulk susceptibility effect of proteins could potentially be observed via signal compartmentalization, image contrast may be attenuated in the volume fraction maps due to field averaging chemical exchange effects.

Methodological considerations

Previous studies have used only a three compartment model (with three parameters for each compartment) defined by white matter characteristics. Our results suggest that the three compartment model is indeed appropriate for white matter (see Tables 2 and 3 and values associated with the corpus callosum). Overall, we found two or three frequency shift compartments for any one brain region studied (Table 2). Hence, the use of a five compartment model with all parameters left free leads to overfitting in all brain regions (see Table 2 and trend in AIC values for model selection). Therefore, interpretation of parameter values generated using a five compartment model with all parameters left free is not straightforward, as parameter values can start to deviate from their expected values through counteraction with other parameters. To compensate for overfitting, we decided to fix frequency shifts, the model parameters linked with biology.

Multi-angle acquisitions were not used in this study. Radial susceptibility anisotropy is thought to result from the orientation of glycolipids and phospholipids with respect to the static magnetic field (He and Yablonskiy, 2009; Lee et al., 2017; Li et al., 2012; Liu, 2010; Wharton and Bowtell, 2012; Xu et al., 2017). Both the anisotropy of tissue and susceptibility could explain the high fitting error observed in white matter structures surrounding the corpus striatum (Fig. 6). This result falls in line with previous reports of high structured errors in white matter regions, arising from the effects of tissue and susceptibility anisotropy on signal frequency dispersion (Alonso-Ortiz et al., 2017; Jongho Lee et al., 2017; van Gelderen et al., 2012; Wharton and Bowtell, 2012; Yablonskiy and Sukstanskii, 2017).

Studies using GRE-MRI signal compartments have investigated the use of non-filtered and filtered phase data (Nam et al., 2015), and used susceptibility maps obtained using a QSM pipeline (Nissi et al., 2015; Sood et al., 2017; Wu et al., 2017). The latter studies suggest that data can be improved using the QSM pipeline by overcoming non-local phase contrast and orientation dependence. Since the QSM pipeline in essence is a phase filter which maps to a quantitative range, it is plausible that residual background fields are present in the data. We used the same QSM pipeline across all echo images, hence any leftover background effects will consistently be present in all echo images. In terms of signal compartmentalization, this can lead to an offset in the compartment frequency shift (refer to Fig. 4 for spreads about identified compartment frequency shifts). Future work should investigate how different QSM pipelines influence the distribution of frequency shifts for each signal compartment.

Our investigation involved nine brains regions segmented manually in individual participants. We opted for this approach to maximize segmentation accuracy. As such, we have not considered all tissue types or classes within the brain. It is therefore plausible that other frequency shift compartments in brain regions not investigated could be present. Future

research could investigate the total number of frequency shift compartments in the human brain with either the use of additional brain regions generated using a segmentation package, or opt to identify them using a purely data driven approach based on voxel-wise fitting across the entire brain.

Conclusions

Our findings suggest the presence of five global signal compartments in the gray and white matter regions investigated. Furthermore, the frequency shift signatures exhibited by these signal compartments are likely to reflect underlying differences in tissue microstructure. Our approach may assist in identifying parametric biomarkers of neurological disorders.

Acknowledgements

The authors extend their gratitude to Dr. Markus Barth and Dr. Reza Bonyadi for providing key technical insights throughout the entirety of the project. Shrinath Kadamangudi received the University of Queensland International Scholarship MPhil scholarship, awarded by the Queensland Brain Institute, for this work. The authors acknowledge the funding received from the Australian Research Council (DP140103593) and from the National Health and Medical Research Council (AP1104933) in support of this project.

ACCEPTED MANUSCRIPT

References

Abduljalil, A.M., Schmalbrock, P., Novak, V., Chakeres, D.W., 2003. Enhanced gray and white matter contrast of phase susceptibility-weighted images in ultra-high-field magnetic resonance imaging. J. Magn. Reson. Imaging 18, 284–290. https://doi.org/10.1002/jmri.10362

Akaike, H., 2011. Akaike's information criterion, in: International Encyclopedia of Statistical Science. Springer, pp. 25–25.

Alonso-Ortiz, E., Levesque, I.R., Pike, G.B., 2017. Impact of magnetic susceptibility anisotropy at 3 T and 7 T on T2*-based myelin water fraction imaging. NeuroImage. https://doi.org/10.1016/j.neuroimage.2017.09.040

Aquino, D., Bizzi, A., Grisoli, M., Garavaglia, B., Bruzzone, M.G., Nardocci, N., Savoiardo, M., Chiapparini, L., 2009. Age-related Iron Deposition in the Basal Ganglia: Quantitative Analysis in Healthy Subjects. Radiology 252, 165–172. https://doi.org/10.1148/radiol.2522081399

Arthur, D., Vassilvitskii, S., 2007. k-means++: The advantages of careful seeding, in: Proceedings of the Eighteenth Annual ACM-SIAM Symposium on Discrete Algorithms. Society for Industrial and Applied Mathematics, pp. 1027–1035.

Bedrick, E.J., Tsai, C.-L., 1994. Model Selection for Multivariate Regression in Small Samples. Biometrics 50, 226. https://doi.org/10.2307/2533213

Bollmann, S., Zimmer, F., O'Brien, F., Vegh, V., Barth, M., 2015. When to perform channel combination in 7 Tesla quantitative susceptibility mapping?, in: Organization of the Human Brain Mapping.

Burnham, K.P., Anderson, D.R., 2004. Multimodel Inference: Understanding AIC and BIC in Model Selection. Sociol. Methods Res. 33, 261–304. https://doi.org/10.1177/0049124104268644

Chen, W.C., Foxley, S., Miller, K.L., 2013. Detecting microstructural properties of white matter based on compartmentalization of magnetic susceptibility. NeuroImage 70, 1–9. https://doi.org/10.1016/j.neuroimage.2012.12.032

Cronin, M.J., Wang, N., Decker, K.S., Wei, H., Zhu, W.-Z., Liu, C., 2017. Exploring the origins of echo-time-dependent quantitative susceptibility mapping (QSM) measurements in healthy tissue and cerebral microbleeds. NeuroImage 149, 98–113. https://doi.org/10.1016/j.neuroimage.2017.01.053

Deistung, A., Schäfer, A., Schweser, F., Biedermann, U., Turner, R., Reichenbach, J.R., 2013. Toward in vivo histology: A comparison of quantitative susceptibility mapping (QSM) with magnitude-, phase-, and R2□-imaging at ultra-high magnetic field strength. NeuroImage 65, 299–314. https://doi.org/10.1016/j.neuroimage.2012.09.055

Drayer, B., Burger, P., Darwin, R., Riederer, S., Herfkens, R., Johnson, G., 1986. MRI of brain iron. Am. J. Roentgenol. 147, 103–110. https://doi.org/10.2214/ajr.147.1.103

Du, Y.P., Chu, R., Hwang, D., Brown, M.S., Kleinschmidt-DeMasters, B.K., Singel, D., Simon, J.H., 2007. Fast multislice mapping of the myelin water fraction using multicompartment analysis ofT2* decay at 3T: A preliminary postmortem study. Magn. Reson. Med. 58, 865–870. https://doi.org/10.1002/mrm.21409

Duyn, J.H., Schenck, J., 2017. Contributions to magnetic susceptibility of brain tissue. NMR Biomed. 30, n/a-n/a. https://doi.org/10.1002/nbm.3546

Duyn, J.H., van Gelderen, P., Li, T.-Q., de Zwart, J.A., Koretsky, A.P., Fukunaga, M., 2007. High-field MRI of brain cortical substructure based on signal phase. Proc. Natl. Acad. Sci. 104, 11796–11801.

Fukunaga, M., Li, T.-Q., Gelderen, P. van, Zwart, J.A. de, Shmueli, K., Yao, B., Lee, J., Maric, D., Aronova, M.A., Zhang, G., Leapman, R.D., Schenck, J.F., Merkle, H.,

Duyn, J.H., 2010. Layer-specific variation of iron content in cerebral cortex as a source of MRI contrast. Proc. Natl. Acad. Sci. 107, 3834–3839. https://doi.org/10.1073/pnas.0911177107

Haacke, E.M., Ayaz, M., Khan, A., Manova, E.S., Krishnamurthy, B., Gollapalli, L., Ciulla, C., Kim, I., Petersen, F., Kirsch, W., 2007. Establishing a baseline phase behavior in magnetic resonance imaging to determine normal vs. abnormal iron content in the brain. J. Magn. Reson. Imaging 26, 256–264. https://doi.org/10.1002/jmri.22987

Hallgren, B., Sourander, P., 1958. The Effect of Age on the Non-Haemin Iron in the Human Brain. J. Neurochem. 3, 41–51. https://doi.org/10.1111/j.1471-4159.1958.tb12607.x

He, X., Yablonskiy, D.A., 2009. Biophysical mechanisms of phase contrast in gradient echo MRI. Proc. Natl. Acad. Sci. 106, 13558–13563.

Hong, F.T., Mauzerall, D., Mauro, A., 1971. Magnetic Anisotropy and the Orientation of Retinal Rods in a Homogeneous Magnetic Field. Proc. Natl. Acad. Sci. U. S. A. 68, 1283–1285.

Hurvich, C.M., Tsai, C.-L., 1989. Regression and time series model selection in small samples. Biometrika 76, 297–307.

Hwang, D., Kim, D.-H., Du, Y.P., 2010. In vivo multi-slice mapping of myelin water content using T2* decay. NeuroImage 52, 198–204. https://doi.org/10.1016/j.neuroimage.2010.04.023

Jessen, N.A., Munk, A.S.F., Lundgaard, I., Nedergaard, M., 2015. The Glymphatic System – A Beginner's Guide. Neurochem. Res. 40, 2583–2599. https://doi.org/10.1007/s11064-015-1581-6

Khalil, M., Riedlbauer, B., Langkammer, C., Enzinger, C., Ropele, S., Stojakovic, T., Scharnagl, H., Culea, V., Petzold, A., Teunissen, C.E., others, 2014. Cerebrospinal fluid transferrin levels are reduced in patients with early multiple sclerosis. Mult. Scler. J. 20, 1569–1577.

Lee, Jongho, Nam, Y., Choi, J.Y., Kim, E.Y., Oh, S.-H., Kim, D.-H., 2017. Mechanisms of T2* anisotropy and gradient echo myelin water imaging. NMR Biomed. 30, n/a-n/a. https://doi.org/10.1002/nbm.3513

Lee, J., Shmueli, K., Kang, B.-T., Yao, B., Fukunaga, M., van Gelderen, P., Palumbo, S., Bosetti, F., Silva, A.C., Duyn, J.H., 2012. The contribution of myelin to magnetic susceptibility-weighted contrasts in high-field MRI of the brain. NeuroImage 59, 3967–3975. https://doi.org/10.1016/j.neuroimage.2011.10.076

Lee, Jingu, Shin, H.-G., Jung, W., Nam, Y., Oh, S.-H., Lee, Jongho, 2017. An R2* model of white matter for fiber orientation and myelin concentration. NeuroImage 162, 269–275. https://doi.org/10.1016/j.neuroimage.2017.08.050

Leutritz, T., Hilfert, L., Smalla, K.-H., Speck, O., Zhong, K., 2013. Accurate quantification of water-macromolecule exchange induced frequency shift: Effects of reference substance. Magn. Reson. Med. 69, 263–268. https://doi.org/10.1002/mrm.24223

Li, W., Avram, A.V., Wu, B., Xiao, X., Liu, C., 2014. Integrated Laplacian-based phase unwrapping and background phase removal for quantitative susceptibility mapping: HARPERELLA PHASE PROCESSING. NMR Biomed. 27, 219–227. https://doi.org/10.1002/nbm.3056

Li, W., Wu, B., Avram, A.V., Liu, C., 2012. Magnetic susceptibility anisotropy of human brain in vivo and its molecular underpinnings. NeuroImage 59, 2088–2097. https://doi.org/10.1016/j.neuroimage.2011.10.038

Li, X., van Gelderen, P., Sati, P., de Zwart, J.A., Reich, D.S., Duyn, J.H., 2015. Detection of demyelination in multiple sclerosis by analysis of T2* relaxation at 7T. NeuroImage Clin. 7, 709–714. https://doi.org/10.1016/j.nicl.2015.02.021

Liu, C., 2010. Susceptibility tensor imaging. Magn. Reson. Med. 63, 1471–1477. https://doi.org/10.1002/mrm.22482

Liu, C., Li, W., Johnson, G.A., Wu, B., 2011. High-field (9.4T) MRI of brain dysmyelination by quantitative mapping of magnetic susceptibility. NeuroImage 56, 930–938. https://doi.org/10.1016/j.neuroimage.2011.02.024

Luo, J., He, X., d'Avignon, D.A., Ackerman, J.J.H., Yablonskiy, D.A., 2010. Protein-induced water 1H MR frequency shifts: Contributions from magnetic susceptibility and exchange effects. J. Magn. Reson. 202, 102–108. https://doi.org/10.1016/j.jmr.2009.10.005

Naik, P.A., Shi, P., Tsai, C.-L., 2007. Extending the Akaike Information Criterion to Mixture Regression Models. J. Am. Stat. Assoc. 102, 244–254. https://doi.org/10.1198/016214506000000861

Nam, Y., Lee, J., Hwang, D., Kim, D.-H., 2015. Improved estimation of myelin water fraction using complex model fitting. NeuroImage 116, 214–221. https://doi.org/10.1016/j.neuroimage.2015.03.081

Nissi, M.J., Tóth, F., Wang, L., Carlson, C.S., Ellermann, J.M., 2015. Improved Visualization of Cartilage Canals Using Quantitative Susceptibility Mapping. PLOS ONE 10, e0132167. https://doi.org/10.1371/journal.pone.0132167

Purves, D.E., Augustine, G.J., Fitzpatrick, D.E., Katz, L.C., others, 1997. Neuroscience.

Reichenbach, J.R., Venkatesan, R., Yablonskiy, D.A., Thompson, M.R., Lai, S., Haacke, E.M., 1997. Theory and application of static field inhomogeneity effects in gradient-echo imaging. J. Magn. Reson. Imaging 7, 266–279.

Sati, P., van Gelderen, P., Silva, A.C., Reich, D.S., Merkle, H., de Zwart, J.A., Duyn, J.H., 2013. Micro-compartment specific T2□ relaxation in the brain. NeuroImage 77, 268–278. https://doi.org/10.1016/j.neuroimage.2013.03.005

Schenck, J.F., Zimmerman, E.A., 2004. High-field magnetic resonance imaging of brain iron: birth of a biomarker? NMR Biomed. 17, 433–445. https://doi.org/10.1002/nbm.922

Schweser, Deistung, A., Gullmar, D., Atterbury, M., Lehr, B.W., Sommer, K., Reichenbach, J.R., 2011a. Non-linear evolution of GRE phase as a means to investigate tissue microstructure. Proc. 19th Int. Soc. Magn. Reson. Med. 4527.

Schweser, Deistung, A., Lehr, B.W., Reichenbach, J.R., 2011b. Quantitative imaging of intrinsic magnetic tissue properties using MRI signal phase: An approach to in vivo brain iron metabolism? NeuroImage 54, 2789–2807. https://doi.org/10.1016/j.neuroimage.2010.10.070

Schweser, F., Deistung, A., Reichenbach, J.R., 2016. Foundations of MRI phase imaging and processing for Quantitative Susceptibility Mapping (QSM). Z. Für Med. Phys. 26, 6–34. https://doi.org/10.1016/j.zemedi.2015.10.002

Schweser, F., Sommer, K., Deistung, A., Reichenbach, J.R., 2012. Quantitative susceptibility mapping for investigating subtle susceptibility variations in the human brain. NeuroImage 62, 2083–2100. https://doi.org/10.1016/j.neuroimage.2012.05.067

Sherman, S.M., 2016. Thalamus plays a central role in ongoing cortical functioning. Nat. Neurosci. 19, 533–541. https://doi.org/10.1038/nn.4269

Snipes, M., Taylor, D.C., 2014. Model selection and Akaike Information Criteria: An example from wine ratings and prices. Wine Econ. Policy 3, 3–9. https://doi.org/10.1016/j.wep.2014.03.001

Sood, S., Urriola, J., Reutens, D., O'Brien, K., Bollmann, S., Barth, M., Vegh, V., 2017. Echo time-dependent quantitative susceptibility mapping contains information on tissue properties. Magn. Reson. Med. 77, 1946–1958. https://doi.org/10.1002/mrm.26281

Straub, S., Schneider, T.M., Emmerich, J., Freitag, M.T., Ziener, C.H., Schlemmer, H.-P., Ladd, M.E., Laun, F.B., 2017. Suitable reference tissues for quantitative susceptibility mapping of the brain: Reference Tissues for QSM of the Brain. Magn. Reson. Med. 78, 204–214. https://doi.org/10.1002/mrm.26369

Thapaliya, K., Vegh, V., Bollmann, S., Barth, M., 2017. Assessment of microstructural signal compartments across the corpus callosum using multi-echo gradient recalled echo at 7 T. NeuroImage. https://doi.org/10.1016/j.neuroimage.2017.11.029

Todorich, B., Pasquini, J.M., Garcia, C.I., Paez, P.M., Connor, J.R., 2009. Oligodendrocytes and myelination: The role of iron. Glia 57, 467–478. https://doi.org/10.1002/glia.20784

van Gelderen, P., de Zwart, J.A., Lee, J., Sati, P., Reich, D.S., Duyn, J.H., 2012. Nonexponential T2* decay in white matter. Magn. Reson. Med. 67, 110–117. https://doi.org/10.1002/mrm.22990

Vandekerckhove, J., Matzke, D., Wagenmakers, E.-J., 2014. Model comparison and the principle of parsimony.

Wharton, S., Bowtell, R., 2012. Fiber orientation-dependent white matter contrast in gradient echo MRI. Proc. Natl. Acad. Sci. 109, 18559–18564. https://doi.org/10.1073/pnas.1211075109

Wu, Z., He, H., Sun, Y., Du, Y., Zhong, J., 2017. High resolution myelin water imaging incorporating local tissue susceptibility analysis. Magn. Reson. Imaging 42, 107–113. https://doi.org/10.1016/j.mri.2017.06.005

Xu, T., Foxley, S., Kleinnijenhuis, M., Chen, W.C., Miller, K.L., 2017. The effect of realistic geometries on the susceptibility-weighted MR signal in white matter. Magn. Reson. Med.

Yablonskiy, D.A., Haacke, E.M., 1994. Theory of NMR signal behavior in magnetically inhomogeneous tissues: The static dephasing regime. Magn. Reson. Med. 32, 749–763. https://doi.org/10.1002/mrm.1910320610

Yablonskiy, D.A., Sukstanskii, A.L., 2017. Effects of biological tissue structural anisotropy and anisotropy of magnetic susceptibility on the gradient echo MRI signal phase: theoretical background: Anisotropy of Magnetic Susceptibility. NMR Biomed. 30, e3655. https://doi.org/10.1002/nbm.3655

Zhong, K., Leupold, J., von Elverfeldt, D., Speck, O., 2008. The molecular basis for gray and white matter contrast in phase imaging. NeuroImage 40, 1561–1566. https://doi.org/10.1016/j.neuroimage.2008.01.061

ACCEPTED MANUSCRIPT